INTERNATIONAL JOURNAL OF CRASHWORTHINESS
2019, VOL. 24, NO. 5, 508–522
https://doi.org/10.1080/13588265.2018.1479482

Taylor & Francis
Taylor & Francis Group

Check for updates

A wave propagation model of distributed energy absorption system for trains

Zhaoyang Ding, Zhijun Zheng and Jilin Yu

CAS Key Laboratory of Mechanical Behavior and Design of Materials, Department of Modern Mechanics, University of Science and Technology of China, Hefei, China

ABSTRACT
The dynamic response of distributed energy absorption system used as a passive safety device in high-speed trains is investigated with a one-dimensional wave propagation model, in which carriages are modelled with elastic rods and energy absorber layers are described by a rigid-perfectly plastic-locking material model. Three collision scenarios are analyzed by taking the stresses and velocities of the interfaces as control variables and a set of ordinary deferential equations is obtained for each stage of collision, the duration of which is the time for the elastic wave to pass from one end of the rod to the other. A platform phenomenon of response in all stages is observed. A simplified approximate analysis procedure is proposed to analyze the energy absorption capability. It is found that ignoring the elastic wave effect of carriages will lead to a wrong estimate of the energy absorption capability and the contribution of individual energy absorber.

ARTICLE HISTORY
Received 7 September 2017
Accepted 17 December 2017

KEYWORDS
Distributed energy absorption system; elastic wave effect; plastic compaction wave; theoretical analysis

1. Introduction

The safety of train operation attracts more and more attention with the development of high-speed trains. The active safety technology was considered as an efficient means for preventing workplace accidents and near accidents [1]. A warning mechanism is built through the study of the relationship between railway accident and its important influencing factors to promote railway safety [2]. However, occasional collision accidents have demonstrated that the active safety technology is too much dependent on the reaction time of drivers. Therefore, the passive safety technology deserves much attention to improve the crashworthiness of train.

An experiment of one athletic actual sized train impacting on a standing one was carried out in France to investigate the climbing of guided transport vehicles during a crash [3]. 'Crash-energy management' technology was designed and the impact energy was absorbed by 'crash zones' located at the ends of each car. With the development of computer technology, theoretical analysis combined with numerical simulation takes the place of experiment and becomes the most commonly used and economical measure to investigate structural crashworthiness of trains [4]. Optimal designs of train structures were given to improve the energy absorption capacity and crashworthiness of trains [5,6]. Gao and Tian [7] provided an optimal design method of trains with strengthening the rigidity of carriage and providing special energy absorbers at the ends of a car. Crash energy management is improved through changing the structure of car-end, which made part of collision energy be absorbed by followed carriages [8–10]. Some investigations were focused on the safety of passengers, which employed dummy to obtain more detailed response of passengers and to assess their safety [11,12]. Researches on materials and structures of energy-absorbing device were carried out and some methods of optimal design were suggested [13–15]. Multibody dynamics and related numerical simulation were widely used for train crash analysis [16–19]. Obviously, researchers have paid much attention to improving the crashworthiness of train and have gained a variety of achievements.

It seems that the existing studies are mainly focused on the design and optimization of single energy-absorbing device, though energy absorbers are distributed at the ends of train carriages. Even for those researches, which take the distributed energy absorption system into consideration, most of them employ rigid-body models to represent carriages in

CONTACT Zhijun Zheng zjzheng@ustc.edu.cn
© 2019 Informa UK Limited, trading as Taylor & Francis Group

numerical simulations. However, a train is a very long structure system with carriages connected with each other. The length of a carriage is about 25 m. When collision occurs, the impact load takes ~5 ms to propagate from the front to the rear of a carriage in the form of elastic wave, and the length involved in the event increases with the passage of time. This means that a considerable portion of an energy absorber would be compressed before the impact load reaches the next one. Hence, in order to assess the efficiency of the energy absorbing system, the effect of stress wave propagation along the train and the coordination between energy absorbers should be considered. Some analysis on collisions of combined plastic rods by theoretical derivation only considering plastic wave effect have been carried out [20,21], but the research where the plastic devices are separated by long sized elastic devices considering elastic wave effect and plastic wave effect simultaneously is rare.

In this study, a theoretical model considering the effect of stress wave propagation is developed. In Section 2, a simplified one-dimensional model is established which takes the distribution of energy absorbing devices and the elasticity of the train carriages into consideration. Three collision scenarios are analyzed. In Section 3, the theoretical results are presented for certain impact scenarios. The results are then verified by finite element method with ABAQUS/Explicit code. In Section 4, the main feature of the response is discussed and a simplified formula for evaluating energy absorption is obtained. The necessity of introducing stress wave effect is then confirmed. Finally, conclusions are given in Section 5.

2. Theoretical analysis

2.1. A simplified theoretical model

The energy absorbing device and carriage body are joined by metal beam and plate structure, which play the roles of structure supporting and load transmission. When collision occurs, the impact load is transmitted through the train from the front end to the rear end, and the energy absorbing devices may be crushed. The load passes through the carriage body, which is mainly a tubular structure, in the form of elastic wave except in the catastrophe cases. To be noticed, the axial action plays a decisive role both in compression failure behaviour of energy absorbing components and in load transfer during collision. Therefore, when neglecting the various influences of the detailed three-dimensional structures on the load

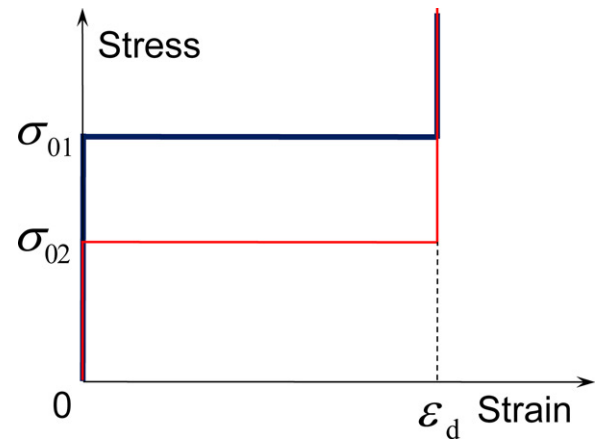

Figure 1. The R-PP-L material model.

transmission and energy absorption, the train can be simplified to a one-dimensional model as elastic rods, which represent the carriages, connected by plastic layers, which represent energy absorbing devices, and can be investigated based on a one-dimensional stress wave theory, only taking the axial effect into consideration.

The energy absorbing device is a structure that can be crushed to absorb impact energy during collision. The size of the energy absorbing device is small and the time of elastic wave propagation in it is rather shorter than that in the carriage. In addition, we are more concerned about the plastic effect rather than the elastic effect of energy absorbing device. Considering the time scales and concerns, we employ the rigid-perfectly plastic-locking (R-PP-L) model [22] to investigate the dynamic response of the materials of energy absorbing device, as shown in Figure 1. The two parameters in the model, that is the plateau stress and the densification strain correspond to the mean crash stress and the stroke efficiency, respectively. On the other hand, linear-elastic material is employed for carriage, assuming that there is no plastic deformation. The simplified model of each carriage with energy absorbers, as shown in Figure 2, is made up of an elastic compartment and an energy absorption layer named as distal layer at the back-end[1]. The front car has an extra energy absorbing layer at the front-end, which is named as proximal layer here.

It is worth noting that the energy-absorbing components in a distributed energy-absorbing system need to meet a certain distribution rule to coordinate with each other. The subsequent energy absorbing components should start work before that at the impact end is fully compacted. To meet this requirement, the plateau stress of proximal layer (σ_{01}) should

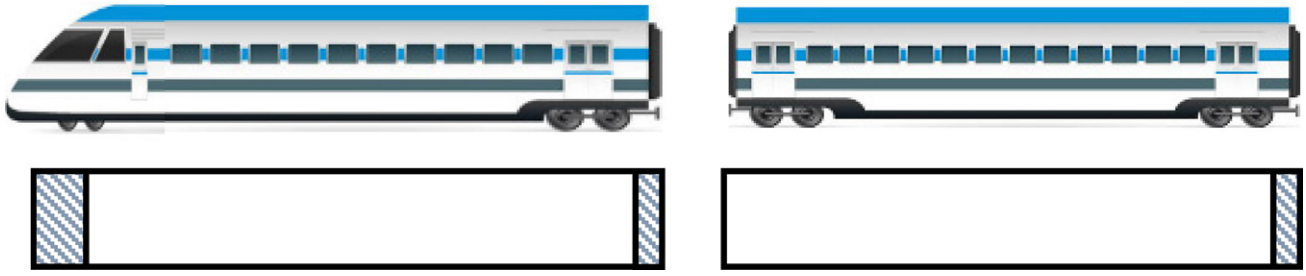

Figure 2. A schematic diagram of the simplified model.

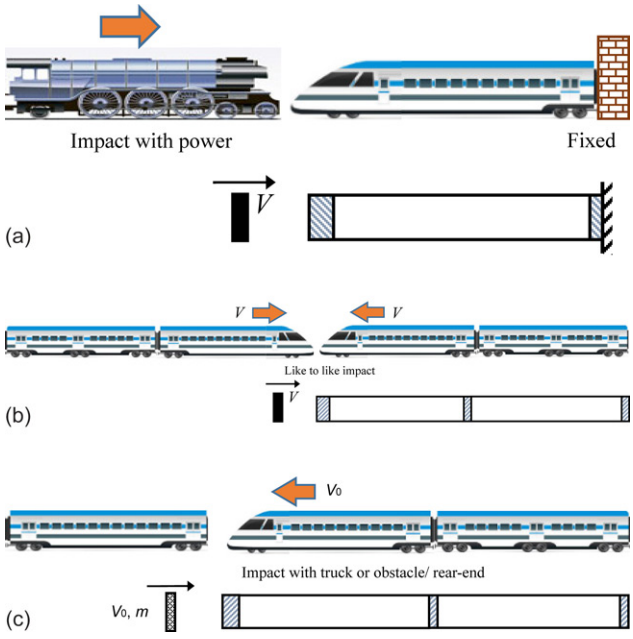

Figure 3. Three collision scenarios of actual train and the corresponding simplified models: (a) Scenario I, (b) Scenario II and (c) Scenario III.

be higher than that of the distal layer (σ_{02}), as shown in Figure 1.

This simplified model is developed to conduct the theoretical analysis of different collision scenarios. By changing the number of cars and collision conditions, a variety of train collision scenarios can be simulated. As shown in Figure 3, three collision scenarios are analyzed in this study: a rigid body impacting on a fixed model of head car with a constant velocity (Scenario I), a rigid body impacting on a combined model of a front car and a carriage, which is set static and free, respectively with a constant velocity (Scenario II) and with an initial velocity (Scenario III). Scenario I represents a power driven train with a constant velocity impacting on a fixed one. Scenario II simulates a 'like to like' impact, in which the two trains with the same initial velocity and mass strike each other. Scenario III can simulate a rear-end collision or impact with a truck or obstacle.

2.2. Theoretical derivations

In this section, all the three collision scenarios are studied to investigate the performance of distributed energy absorption system during collision. The equations of motion are based on the Lagrangian coordinates.

The parameters of the energy absorption layers used in the analysis of the simplified model are: the plateau stress σ_{01} and σ_{02} are 150 and 100 MPa, respectively; the density and length of the proximal layer are $\rho_1 = 600\,\mathrm{kg\,m^{-3}}$ and $L_1 = 1$ m, and those of the distal layer are $\rho_2 = 400\,\mathrm{kg\,m^{-3}}$ and $L_2 = 0.5$ m; the compaction strain is $\varepsilon_d = 0.8$; the length of the elastic rod is $L_0 = 25$ m, which has a Young's modulus $E = 66$ GPa and a density $\rho_0 = 2700\,\mathrm{kg\,m^{-3}}$. In Scenario I and Scenario II, a constant impact velocity $V = 20\,\mathrm{m\,s^{-1}}$ is applied, while in Scenario III, the initial velocity of the impact block is set as $V_0 = 20\ \mathrm{m\,s^{-1}}$.

During collision, the elastic wave propagation is the key for the load and impact energy transmissions between the proximal layer and the distal layer. The analysis process is divided into several stages by the characteristic time t_n ($n = 1, 2, \ldots$) when elastic waves reach corresponding interfaces. The characteristic time t_n meets

$$t_n = nL_0/C_0, \tag{1}$$

where C_0 is the elastic wave speed, given by

$$C_0 = \sqrt{E/\rho_0}. \tag{2}$$

2.2.1. Scenario I

A schematic diagram of simplified model and deformation process of Scenario I is presented in Figure 4.

2.2.1.1. Stage 1 ($0 < t < t_1$). When the rigid block hits the front end, the proximal layer begins to collapse and a compaction wave starts to propagate in the proximal layer. The stress immediate ahead of the compaction wave front becomes σ_{01} which drives the rigid part of the proximal layer forward and

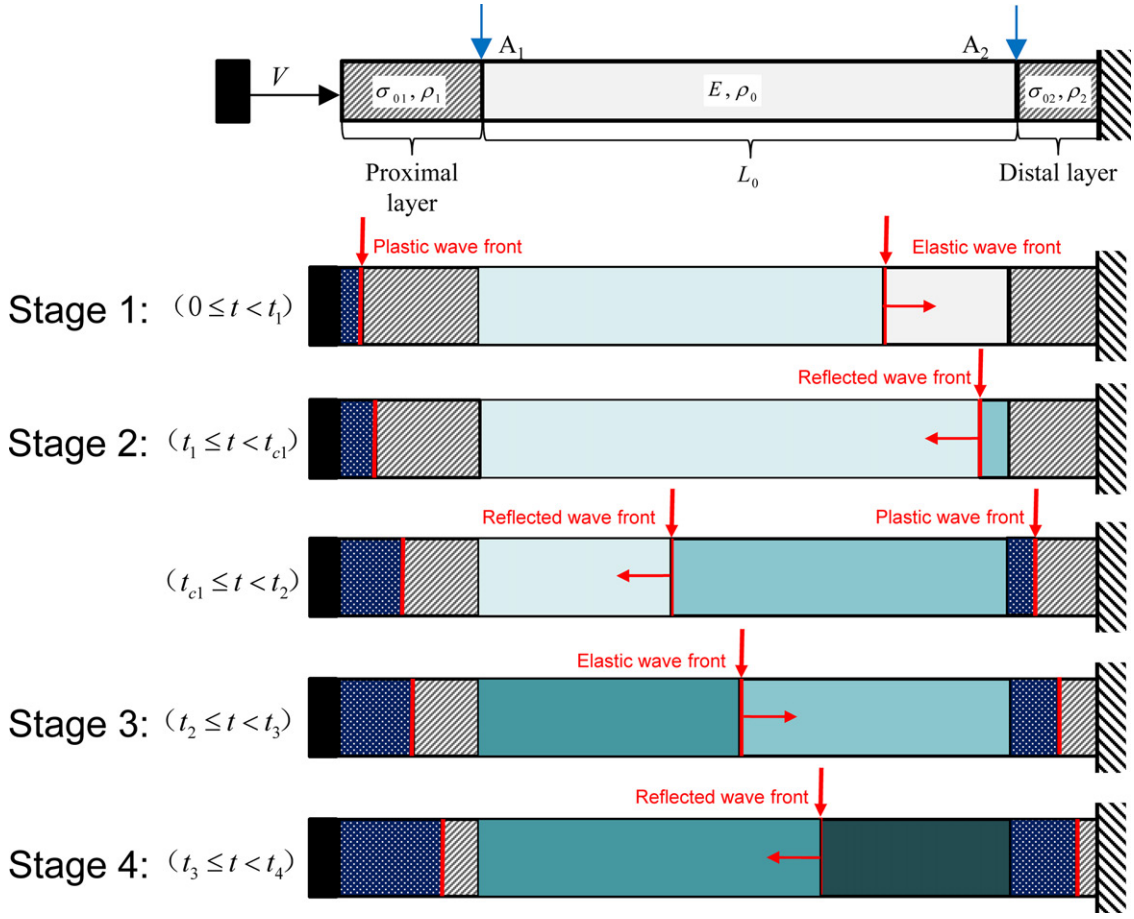

Figure 4. A schematic diagram of simplified model for Scenario I.

accelerates it immediately. According to the elastic wave theory, as the velocity of interface A_1 increases, the stress on interface A_1 rises and approaches σ_{01}. Simultaneously, an elastic wave initiates and travels from interface A_1 to interface A_2 through the elastic rod at speed C_0. Before the wave reaches interface A_2 at t_1, the distal layer remains undeformed.

For interface A_1, the stress σ_{A1} can be expressed by the interfacial velocity. Using the compatibility relation of elastic wave

$$d\sigma_{A1} = \frac{E}{C_0}\, dv_{R1} \tag{3}$$

and the initial condition $v_{R1}(0) = 0$ and $\sigma_{A1}(0) = 0$, we have

$$\sigma_{A1} = \frac{E}{C_0}\, v_{R1}, \tag{4}$$

where v_{R1} is the particle velocity at interface A_1 associated to the right-travelling wave from interface A_1.

The conservation of the mass of the proximal layer gives

$$\frac{d\Phi_1^{(1)}}{dt} = \frac{V - v_{R1}^{(1)}}{\varepsilon_d}, \tag{5}$$

where Φ_1 is the compaction length of the proximal layer. In addition, applying the momentum theorem to the undeformed region of proximal layer and using Eq. (4), we obtain

$$\frac{dv_{R1}^{(1)}}{dt} = \frac{\sigma_{01} - E v_{R1}^{(1)}/C_0}{\rho_1\left(L_1 - \Phi_1^{(1)}\right)}, \tag{6}$$

where superscript (n) denotes the nth stage of the response ($n = 1, 2, \ldots$).

Equations (5) and (6) together with the initial conditions $\Phi_1^{(1)}(0) = 0$ and $v_{R1}^{(1)}(0) = 0$ are the governing equations which controls the response during Stage 1. Because there is only a right-travelling simple wave, once the particle velocity v_{R1} is solved, together with the corresponding stress on interface A_1 given by Eq. (4), the wave motion in the elastic rod is obtained.

2.2.1.2. Stage 2 ($t_1 < t < t_2$). After the elastic wave reaches interface A_2, a reflected wave begins to propagate to the left, which is called a left-travelling wave. The velocity and stress of interface A_2 are determined by superposition of the two simple waves, that is the right-travelling wave and the left-travelling wave.

When the stress of interface A_2 reaches σ_{02}, the distal layer begins to be crushed and absorbing energy from this moment.

The response of interface A_2 due to the right-travelling wave is corresponding to that of interface A_1 with only a time delay of Δt as

$$\Delta t = L_0/C_0. \tag{7}$$

So the velocity and stress of interface A_2 can be expressed as

$$v_{A2}^{(2)}(t) = v_{R1}^{(1)}(\bar{t}) + v_{L1}^{(2)}(t) \tag{8}$$

and

$$\sigma_{A2}^{(2)}(t) = \sigma_{R1}^{(1)}(\bar{t}) + \sigma_{L1}^{(2)}(t), \tag{9}$$

respectively, where

$$\bar{t} = t - \Delta t \tag{10}$$

and v_{L1} and σ_{L1} are the particle velocity and stress at interface A_2 associated to the left-travelling wave from interface A_2.

For a short period of time, σ_{A2} is lower than σ_{02} and the distal layer remains undeformed and stationary, the right-travelling wave reflects from the rigid surface A_2, so we have

$$v_{L1}^{(2)}(t) = -v_{R1}^{(1)}(\bar{t}), \quad v_{A2}^{(2)}(t) = 0, \tag{11}$$

and

$$\sigma_{L1}^{(2)}(t) = \sigma_{R1}^{(1)}(\bar{t}), \sigma_{A2}^{(2)}(t) = 2\sigma_{R1}^{(1)}(\bar{t}) \tag{12}$$

The time when σ_{A2} reaches σ_{02}, denoted as t_{c1}, can be determined from Eq. (12). Afterward, the distal layer begins to collapse and a compaction wave starts to propagate in the distal layer. The materials ahead of and behind the wave front remain rigid, so the particle velocity just ahead of the compaction wave front is zero while that just behind the front is equal to that of interface A_2, that is $v_{A2}^{(2)}(t)$ From the conservation condition of mass across the collapse wave front and using Eq. (8), we have

$$\frac{d\Phi_2^{(2)}}{dt} = \frac{v_{R1}^{(1)}(\bar{t}) + v_{L1}^{(2)}(t)}{\varepsilon_d}, \tag{13}$$

where Φ_2 is the compaction length of the distal layer. In addition, the kinetic compatibility condition can be obtained from the conservation of momentum across the wave front and expressed as

$$\sigma_2^{(2)}(t) - \sigma_{02} = \rho_2 \frac{d\Phi_2^{(2)}}{dt} v_{A2}^{(2)}(t), \tag{14}$$

where $\sigma_2^{(2)}(t)$ is the stress just behind the collapsing wave front in the distal layer. Equations (13) and (14) with using Eq. (8) lead to

$$\sigma_2^{(2)}(t) = \sigma_{02} + \rho_2 \left(v_{L1}^{(2)}(t) + v_{R1}^{(1)}(\bar{t}) \right)^2 / \varepsilon_d. \tag{15}$$

Applying the momentum theorem to the compacted region of the distal layer, together with Eq. (15), gives

$$\frac{dv_{L1}^{(2)}}{dt} = \frac{E\left(v_{L1}^{(2)}(t) + v_{R1}^{(1)}(\bar{t})\right)/C_0 - \sigma_{02} - \rho_2\left(v_{L1}^{(2)}(t) + v_{R1}^{(1)}(\bar{t})\right)^2/\varepsilon_d}{\rho_2 \Phi_2^{(2)}(t)} - \frac{dv_{R1}^{(1)}(\bar{t})}{dt}. \tag{16}$$

Equations (13) and (16) together with the initial conditions $\Phi_2^{(2)}(t_{c1}) = 0$ and $v_{L1}^{(2)}(t_{c1}) = -C_0\sigma_{02}/2E$ are the governing equations for Stage 2. It is worth noting that $v_{R1}^{(1)}(\bar{t})$ is known, because the solutions for Stage 1 have been obtained.

It should be noted that the equations of motion of the proximal layer stay unchanged in Stage 2, because there is no new wave arriving at interface A_1. In the analysis of subsequent stages, only new equations of motion will be shown.

2.2.1.3. Stage 3 ($t_2 < t < t_3$). The left-travelling wave reaches interface A_1 at t_2, then the velocity response of interface A_1 depends on the superposition of left-travelling wave and a new right-travelling wave, which causes the equations of motion to be different from those of Stage 1and can be written as

$$\frac{d\Phi_1^{(3)}}{dt} = \frac{V - \left(v_{R1}^{(3)}(t) + v_{L1}^{(2)}(\bar{t})\right)}{\varepsilon_d} \tag{17}$$

and

$$\frac{dv_{R1}^{(3)}}{dt} = \frac{\sigma_{01} - E\left(v_{R1}^{(3)}(t) - v_{L1}^{(2)}(\bar{t})\right)/C_0}{\rho_1\left(L_1 - \Phi_1^{(3)}(t)\right)} - \frac{dv_{L1}^{(2)}(\bar{t})}{dt}. \tag{18}$$

where $v_{L1}^{(2)}(\bar{t})$ is known after the response of Stage 2 is obtained. The initial conditions for Eqs. (17) and (18) are $\Phi_1^{(3)}(t_2) = \Phi_1^{(1)}(t_2)$ and $v_{R1}^{(3)}(t_2) = v_{R1}^{(1)}(t_2) + v_{L1}^{(2)}(t_2 - \Delta t)$, respectively.

2.2.1.4. Stage 4 ($t_3 < t < t_4$). In Stage 4, a new left-travelling wave initiated at interface A_2 due to the reflection of the right-travelling wave, similar to Stage 2 shown in Figure 2. Hence the governing equations for this stage are similar to those in Stage 2, except that $v_{L1}^{(2)}$ is replaced by $v_{L1}^{(4)}$ in the equations of motion. We have

$$\frac{d\Phi_2^{(4)}}{dt} = \frac{v_{L1}^{(4)}(t) + v_{R1}^{(3)}(\bar{t})}{\varepsilon_d} \tag{19}$$

and

$$\frac{dv_{L1}^{(4)}}{dt} = \frac{E\left(v_{L1}^{(4)}(t) + v_{R1}^{(3)}(\bar{t})\right)/C_0 - \sigma_{02} - \rho_2\left(v_{L1}^{(4)}(t) + v_{R1}^{(3)}(\bar{t})\right)^2/\varepsilon_d}{\rho_2\Phi_2^{(4)}(t)} - \frac{dv_{R1}^{(3)}(\bar{t})}{dt}, \tag{20}$$

with the initial conditions $\Phi_2^{(4)}(t_3) = \Phi_2^{(2)}(t_3)$ and $v_{L1}^{(4)}(t_3) = v_{R1}^{(3)}(t_3 - \Delta t) - C_0\sigma_{02}/E$.

For the theoretical derivations of all three scenarios, just the first four stages are demonstrated. The derivations for more stages can be obtained following similar rules. For a certain model, the number of stages the collision process required before the end of energy absorption is certain, which will be discussed later.

2.2.2. Scenario II

The theoretical model for Scenario II and the deformation process is schematically presented in Figure 5.

2.2.2.1. Stage 1 ($0 < t < t_1$). In this stage, a compaction wave starts to propagate in the proximal layer and an elastic wave travels from interface A_1 to interface A_2, while the other part of the system remains stationary. So, the governing equations are identical to Eqs. (5) and (6), with corresponding initial conditions.

2.2.2.2. Stage 2 ($t_1 \le t < t_2$). When the elastic wave reaches interface A_2, a reflected wave begins to propagate to the left. Meanwhile, an elastic wave travels through the distal layer I with infinite speed. Different from Scenario I, Interface A_3 starts to move and an elastic wave propagates to the right. Originally, σ_{A2} is lower than σ_{02} and the distal layer I accelerates to the right as a whole, so the velocity and stress of surface A_2 and A_3 are

$$v_{A2}^{(2)}(t) = v_{R1}^{(1)}(\bar{t}) + v_{L1}^{(2)}(t), \sigma_{A2}^{(2)}(t) = E\left(v_{R1}^{(1)}(\bar{t}) - v_{L1}^{(2)}(t)\right)/C_0 \tag{21}$$

and

$$v_{A3}^{(2)} = v_{A2}^{(2)}, \sigma_{A3}^{(2)}(t) = E\left(v_{R1}^{(1)}(\bar{t}) + v_{L1}^{(2)}(t)\right)/C_0 \tag{22}$$

respectively.

The equation of motion is obtained by using the momentum theorem to the distal layer I together with Eqs. (21) and (22) as

$$\frac{dv_{L1}^{(2)}}{dt} = -\frac{2Ev_{L1}^{(2)}(t)}{C_0\rho_2 L_2} - \frac{dv_{R1}^{(1)}(\bar{t})}{dt} \tag{23}$$

with the initial condition $v_{L1}(t_1) = 0$.

When σ_{A2} reaches σ_{02} at t_{c2}, which can be determined from Eqs. (21) and (23), the distal layer I begins to be crushed and a compaction wave starts to propagate in the distal layer I. The situation of the layer is similar to that of Stage 2 of Scenario I except

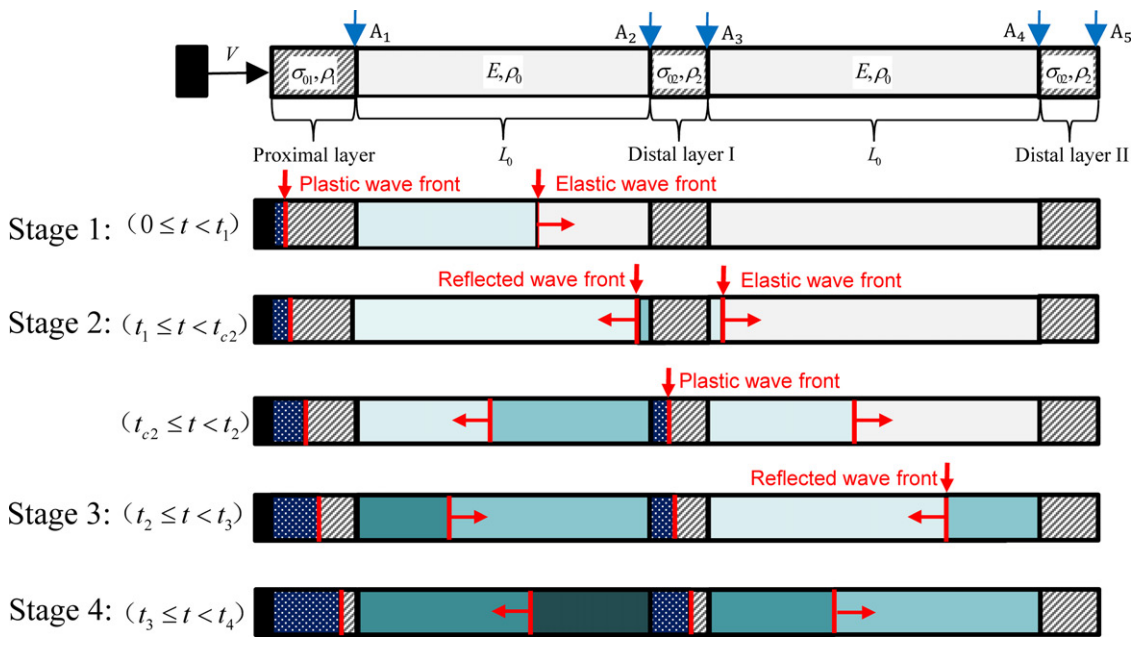

Figure 5. A schematic diagram of simplified model for Scenario II.

that the undeformed part is no longer stationary. From the conservation condition of mass across the collapse wave front, we have

$$\frac{\mathrm{d}\Phi_2^{(2)}}{\mathrm{d}t} = \frac{v_{\mathrm{L1}}^{(2)}(t) + v_{\mathrm{R1}}^{(1)}(\bar{t}) - v_{\mathrm{R2}}^{(2)}(t)}{\varepsilon_{\mathrm{d}}}, \tag{24}$$

where v_{R2} is the particle velocity at interface A_3 associated to the right-travelling wave from interface A_3.

Similar to the analysis for the distal layer in Stage 2 of Scenario I, the particle velocities ahead of and behind the collapse wave front are equal to those at interfaces A_3 and A_2, respectively, and the stress just ahead of the collapse wave front is σ_{02}. From the conservation condition of momentum across the collapse wave front and Eq. (24), the stress just behind the collapsing wave front in the distal layer I can be determined that

$$\sigma_2^{(2)} = \sigma_{02} + \rho_2\left(v_{\mathrm{L1}}^{(2)}(t) + v_{\mathrm{R1}}^{(1)}(\bar{t}) - v_{\mathrm{R2}}^{(2)}(t)\right)^2/\varepsilon_{\mathrm{d}}. \tag{25}$$

By employing the momentum theorem to the deformed and undeformed region of the distal layer I respectively, we have

$$\frac{\mathrm{d}v_{\mathrm{L1}}^{(2)}}{\mathrm{d}t} = -\frac{\frac{E}{C_0}\left(V_{\mathrm{L1}}^{(2)}(t) - v_{\mathrm{R1}}^{(1)}(\bar{t})\right) + \sigma_{02} + \frac{\rho_2}{\varepsilon_{\mathrm{d}}}\left(v_{\mathrm{L1}}^{(2)}(t) + v_{\mathrm{R1}}^{(1)}(\bar{t}) - v_{\mathrm{R2}}^{(2)}(t)\right)^2}{\rho_2\Phi_2^{(2)}(t)} - \frac{\mathrm{d}v_{\mathrm{R1}}^{(1)}(\bar{t})}{\mathrm{d}t} \tag{26}$$

and

$$\frac{\mathrm{d}v_{\mathrm{R2}}^{(2)}}{\mathrm{d}t} = \frac{\sigma_{02} - Ev_{\mathrm{R2}}^{(2)}/C_0}{\rho_2\left(L_1 - \Phi_2^{(2)}\right)}, \tag{27}$$

where Eq. (25) is used.

Equations (24), (26) and (27) together with the initial conditions $\Phi_2^{(2)}(t_{c2}) = 0$, $v_{\mathrm{L1}}^{(2)}(t_{c2}) = v_{\mathrm{R1}}^{(1)}(t_{c2} - \Delta t) - C_0\sigma_{02}/E$ and $v_{\mathrm{R2}}^{(2)}(t_{c2}) = 2v_{\mathrm{R1}}^{(1)}(t_{c2} - \Delta t) - C_0\sigma_{02}/E$ are the governing equations for Stage 2.

2.2.2.3. Stage 3 ($t_2 \le t < t_3$). In this stage, the left-travelling wave propagating in the first elastic rod reaches interface A_1 at t_2 and the analysis process and governing equations for proximal layer are just the same as those of Stage 3 of Scenario I.

The right-travelling wave propagating in the second elastic rod reaches interface A_4 at t_2 and a reflected wave begins to propagate to the left. The distal layer II accelerates to the right without crushing since the plateau stresses of the two distal layers are equal, so the velocity and stress of surface A_4 and A_5, respectively are

$$v_{\mathrm{A4}}^{(3)}(t) = v_{\mathrm{R2}}^{(2)}(\bar{t}) + v_{\mathrm{L2}}^{(3)}(t), \sigma_{\mathrm{A4}}^{(3)}(t) = E\left(v_{\mathrm{R2}}^{(2)}(\bar{t}) - v_{\mathrm{L2}}^{(3)}(t)\right)/C_0 \tag{28}$$

and

$$v_{\mathrm{A5}}^{(3)} = v_{\mathrm{A4}}^{(3)}, \sigma_{\mathrm{A5}} = 0 \tag{29}$$

where v_{L2} is the particle velocity at interface A_4 associated to the left-travelling wave from interface A_4. Applying the momentum theorem to the trailing layer with Eqs. (28) and (29), we have the governing equation

$$\frac{\mathrm{d}v_{\mathrm{L2}}^{(3)}}{\mathrm{d}t} = \frac{E\left(v_{\mathrm{R2}}^{(2)}(\bar{t}) - v_{\mathrm{L2}}^{(3)}(t)\right)}{C_0\rho_2 L_2} - \frac{\mathrm{d}v_{\mathrm{R2}}^{(2)}(\bar{t})}{\mathrm{d}t} \tag{30}$$

with the initial condition $v_{\mathrm{L2}}^{(3)}(t_2) = 0$.

2.2.2.4. Stage 4 ($t_3 \le t < t_4$). The new right-travelling wave reaches interface A_2 and the reflected wave from the distal layer II reaches interface A_3 at t_3. The response of interface A_3 in this stage depends on the superposition of the two simple waves, which is the only difference from that of Stage 2 where only a right-travelling wave exists. Therefore, the governing equations can be expressed as

$$\frac{\mathrm{d}\Phi_2^{(4)}}{\mathrm{d}t} = \frac{v_{\mathrm{R1}}^{(3)}(\bar{t}) + v_{\mathrm{L1}}^{(4)}(t) - \left(v_{\mathrm{R2}}^{(4)}(t) + v_{\mathrm{L2}}^{(3)}(\bar{t})\right)}{\varepsilon_{\mathrm{d}}}, \tag{31}$$

$$\frac{\mathrm{d}v_{\mathrm{L1}}^{(4)}}{\mathrm{d}t} = -\frac{\frac{E}{C_0}\left(v_{\mathrm{L1}}^{(4)}(t) - v_{\mathrm{R1}}^{(3)}(\bar{t})\right) + \sigma_{02} + \frac{\rho_2}{\varepsilon_{\mathrm{d}}}\left(v_{\mathrm{L1}}^{(4)}(t) + v_{\mathrm{R1}}^{(3)}(\bar{t}) - v_{\mathrm{R2}}^{(4)}(t) - v_{\mathrm{L2}}^{(3)}(\bar{t})\right)^2}{\rho_2\Phi_2^{(4)}(t)} - \frac{\mathrm{d}v_{\mathrm{R1}}^{(3)}(\bar{t})}{\mathrm{d}t} \tag{32}$$

and

$$\frac{\mathrm{d}v_{\mathrm{R2}}^{(4)}}{\mathrm{d}t} = \frac{\sigma_{02} - E\left(v_{\mathrm{R2}}^{(4)}(t) - v_{\mathrm{L2}}^{(3)}(\bar{t})\right)/C_0}{\rho_2\left(L_2 - \Phi_2^{(4)}(t)\right)}, \tag{33}$$

with the initial conditions $\Phi_2^{(4)}(t_3) = \Phi_2^{(3)}(t_3)$, $v_{\mathrm{L1}}^{(4)}(t_3) = v_{\mathrm{R1}}^{(3)}(t_3 - \Delta t) - C_0\sigma_{02}/E$ and $v_{\mathrm{R2}}^{(4)}(t_3) = v_{\mathrm{R2}}^{(2)}(t_3) + v_{\mathrm{L2}}^{(3)}(t_3 - \Delta t)$.

2.2.3. Scenario III

For Scenario III shown in Figure 6, the specific mass of the impact block is denoted as m. There is a slowdown of the impact velocity, but it has no influence on the analysis of the two distal layers. Therefore, the governing equations for the distal layers are the same as those of Scenario II, which will not be present here. The derivation of governing equations for Stage 1 and those

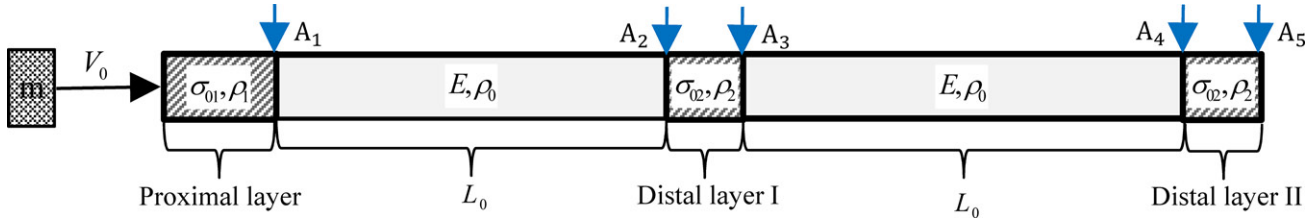

Figure 6. A schematic diagram of simplified model for Scenario III.

related to the proximal layer for Stage 3 is demonstrated here. Similar rules can be used for more stages.

2.2.3.1. Stage 1 ($0< t < t_1$). The velocity of the mass block V is now a new variable to be solved. Similarly, to the analysis of the response of the proximal layer for Scenarios I and II, the governing equations can be obtained by using the conservation conditions of mass and momentum across the collapsing wave front, the momentum theorem for the deformed and undeformed regions of the proximal layer. We have

$$\frac{\mathrm{d}\Phi_1^{(1)}}{\mathrm{d}t} = \frac{V^{(1)} - v_{\mathrm{R1}}^{(1)}}{\varepsilon_{\mathrm{d}}}, \tag{34}$$

$$\frac{\mathrm{d}V^{(1)}}{\mathrm{d}t} = -\frac{\sigma_{01} + \rho_1\left(V^{(1)} - v_{\mathrm{R1}}^{(1)}\right)^2/\varepsilon_{\mathrm{d}}}{m + \Phi_1^{(1)}\rho_1} \tag{35}$$

and

$$\frac{\mathrm{d}v_{\mathrm{R1}}^{(1)}}{\mathrm{d}t} = \frac{\sigma_{01} - Ev_{\mathrm{R1}}^{(1)}/C_0}{\rho_1\left(L_1 - \Phi_1^{(1)}\right)}, \tag{36}$$

with the initial conditions $\Phi_1^{(1)}(0) = 0$, $V^{(1)}(0) = V_0$ and $v_{R1}^{(1)}(0) = 0$.

2.2.3.2. Stage 3 ($t_2 \le t < t_3$). The governing equations are obtained by the same principles as Stage 1 of Scenario III, just additionally taking superposition of the elastic waves at interface A_1 into consideration, and given by

$$\frac{\mathrm{d}\Phi_1^{(3)}}{\mathrm{d}t} = \frac{V^{(3)} - \left(v_{\mathrm{R1}}^{(3)}(t) + v_{\mathrm{L1}}^{(2)}(\bar{t})\right)}{\varepsilon_{\mathrm{d}}}, \tag{37}$$

$$\frac{\mathrm{d}V^{(3)}}{\mathrm{d}t} = -\frac{\sigma_{01} + \rho_1\left[V^{(3)}(t) - \left(v_{\mathrm{R1}}^{(3)}(t) + v_{\mathrm{L1}}^{(2)}(\bar{t})\right)\right]^2/\varepsilon_{\mathrm{d}}}{m + \rho_1\Phi_1^{(3)}(t)} \tag{38}$$

and

$$\frac{\mathrm{d}v_{\mathrm{R1}}^{(3)}}{\mathrm{d}t} = \frac{\sigma_{01} - E\left(v_{\mathrm{R1}}^{(3)}(t) - v_{\mathrm{L1}}^{(2)}(\bar{t})\right)/C_0}{\rho_1\left(L_1 - \Phi_1^{(3)}(t)\right)} - \frac{\mathrm{d}v_{\mathrm{L1}}^{(2)}(\bar{t})}{dt}, \tag{39}$$

with the initial conditions $\Phi_1^{(3)}(t_2) = \Phi_1^{(1)}(t_2)$, $V^{(3)}(t_2) = V^{(1)}(t_2)$ and $v_{\mathrm{R1}}^{(3)}(t_2) = v_{\mathrm{R1}}^{(1)}(t_2) + v_{\mathrm{L1}}^{(2)}(t_2 - \Delta t)$.

2.2.4. Summary of theoretical derivations

It can be seen that even for the simplified model consists only elastic rods and rigid-perfectly plastic-locking layers, the theoretical analysis of the responses is very complicated due to the coupling of elastic and plastic waves. However, taking the advantage of the simple elastic wave propagation, we can divide the analysis process into several stages. In each stage, the wave propagation in a rod can be treated as a superposition of a right-travelling wave and a left-travelling wave, if there is any. Thus, only the stress and particle velocity histories at the interfaces need to be solved. On the other hand, the deformation part and the undeformed part of an energy absorbing layer can be regarded as two rigid bodies, for which the Newton's law of motion or the momentum theorem can be used. In addition, the conservation conditions of mass and momentum across the wave front are used to deal with the propagation of the compaction wave front in an energy absorbing layer.

Thus, the complex problem has been simplified and we just need to solve the stresses and particle velocities at the corresponding interfaces associated to the elastic waves propagating from these interfaces. This method can be extended to other collision scenarios and the governing equations for the impact response of any simplified system can be obtained and solved stage by stage.

3. Results

The fourth-order Runge-Kutta scheme is employed to solve the governing equations given above for Scenario I and Scenario II. For Scenario III, the results are not discussed in this study, because the contribution of the distributed energy absorption system is not fully revealed. The results are then verified by finite element method using ABAQUS/Explicit code.

3.1. Characteristic phenomena in Scenario I

For Scenario I, the calculation is carried out until the stage right after the proximal layer finishes absorbing

energy. Typical time histories of the velocities and stresses of interfaces A_1 and A_2 are shown in Figure 7. As can be seen from the results, the velocities of the two interfaces can be described by several stages and keep almost constant during each stage. The velocities of interface A_1 and A_2 change once every two stages, corresponding to the time duration for an elastic wave travelling forth and back between the two interfaces. The stresses of the two interfaces keep almost constant during collision but the stress of interface A_1 drops down when crushing stops.

Because the Lagrangian speed of the compaction wave in the two energy absorption layers depends on the interface velocity, it is expected that the Lagrangian speeds of the compaction wave in the two layers will also exhibit staged phenomenon, as shown in Figure 8.

For the R-PP-L shock model is employed to investigate the response of materials in the two layers, we consider that the part swept by compaction wave become compacted at once. Afterward the absorbed energy of the two layers can be obtained by

$$E_1 = \int_0^{T_1} \sigma_1 s \dot{\Phi}_1 \varepsilon_d \mathrm{d}t \tag{40}$$

and

$$E_2 = \int_0^{T_2} \sigma_2 s \dot{\Phi}_2 \varepsilon_d \mathrm{d}t, \tag{41}$$

where E_1 and E_2 are absorbed energy of the proximal layer and distal layer respectively, T_1 and T_2 are the times associated to the end of energy absorption for the two layers respectively, σ_1 is the stress just behind the collapsing wave front in the proximal layer and can be solved similarly as σ_2, s is the sectional area of the rod and set as 0.01 m^2. The results of absorbed energy are shown in Figure 9.

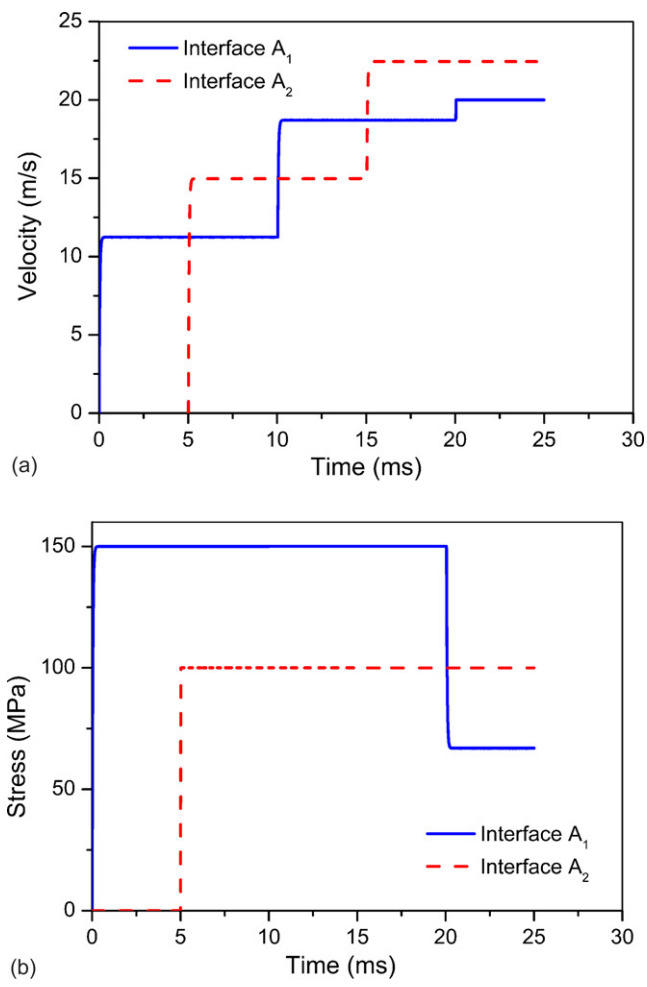

Figure 7. Variation of the velocities (a) and stresses (b) of interfaces A1 and A2.

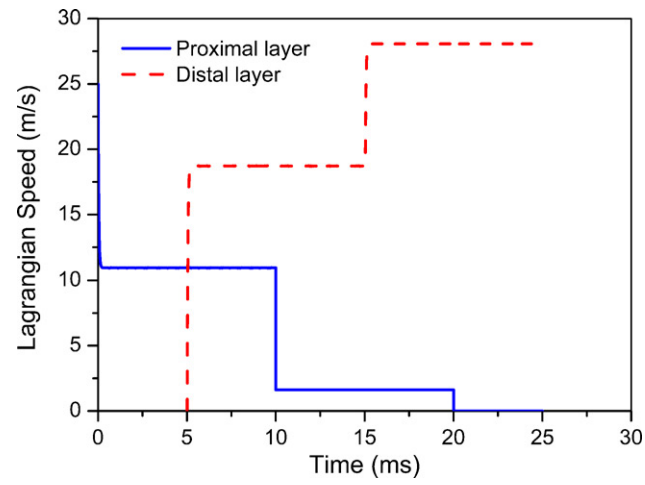

Figure 8. Variation of the Lagrangian speeds of the compaction wave in the proximal layer and the distal layer.

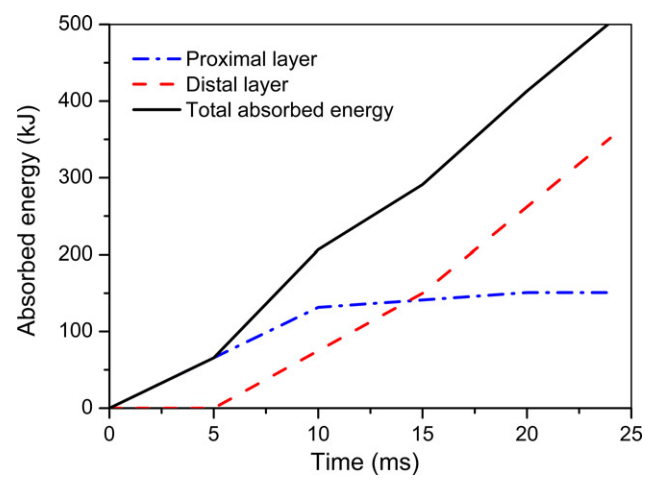

Figure 9. Time histories of absorbed energy in Scenario I.

3.2. Characteristic phenomena in Scenario II

The end of calculation for Scenario II is set when all the energy absorbing layers stop crushing. Typical velocity-time histories and stress-time histories of the three interfaces A_1, A_2 and A_3 are shown in Figure 10. As we can see, the velocity-time histories of interfaces A_1 and A_2 are almost the same as that of Scenario I, both in values and in trends. The velocity of interface A_3 demonstrates also similar features. The velocities of the three interfaces keep almost constant in each stage and change once every two stages. This is a typical feature of the three interfaces.

The time history of Lagrangian speeds of the compaction wave in the proximal layer and distal layer I are shown in Figure 11. The absorbed energy of proximal layer and distal layer I can then be calculated using Eqs. (40) and (41), as shown in Figure 12.

The velocity and stress in the elastic rods are resulted from the superposition of right-travelling and left-travelling elastic waves in each stage. The time histories of velocity and stress for Scenario II at selected Lagrangian locations in the first elastic rod are shown in Figure 13, which also reflects the stepwise response feature of the two corresponding interfaces.

3.3. Validation through finite element simulation

Finite element (FE) method with ABAQUS/Explicit code is employed to verify the theoretical results, taking Scenario II as an example. The FE model is set up with the same dimension parameters, material parameters and collision conditions as in the theoretical model of Scenario II. The constitutive behavior of the materials of the absorbing layers and the elastic connecting rods are respectively based on the crushable foam material model and linear elastic material model. Both the energy absorbing layers and the elastic connecting rods are modeled with C3D8 solid elements, of which the average length is set to be 1 cm through a mesh sensitivity analysis. General contact is defined with zero friction. The boundary conditions which restrict rotation and the movement of the

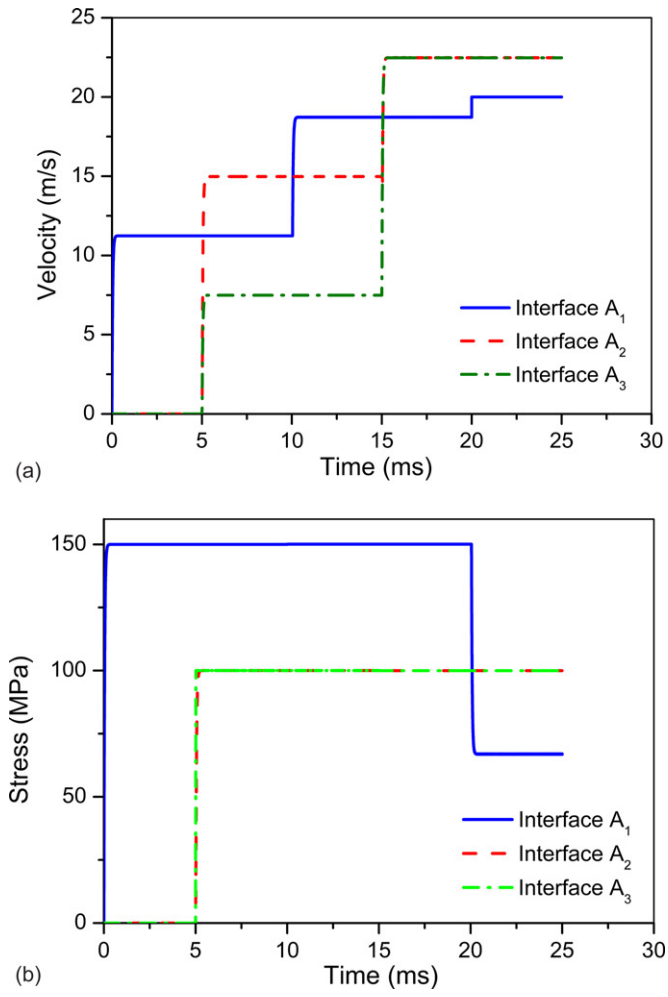

Figure 10. Typical velocity-time histories (a) and stress-time histories (b) of interfaces A1, A2 and A3.

nonaxial directions are imposed. The operation time is set as 25 ms predicted by the theoretical analysis.

The velocity and stress in the elastic rods are resulted from the superposition of right-traveling and left-traveling elastic waves in each stage. To investigate the wave propagation in carriages, a comparison between the theoretical predictions and FE results of velocity and stress at selected Lagrangian locations in the first elastic rod are shown in Figure 14. The solid line is the theoretical prediction for the midpoint. The dotted lines are FE results for the four selected Lagrangian locations.

A comparison between the theoretical prediction and FE results of the absorbed energy of the proximal layer and distal layer I is present in Figure 15, to investigate the process of energy absorption.

The observed agreement presented in Figures 14 and 15 between the theoretical predictions and the FE results verifies the proposed theoretical approach.

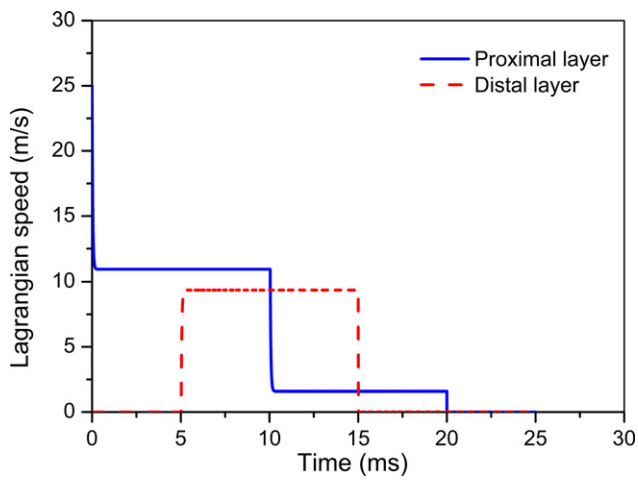

Figure 11. Lagrangian speeds of the compaction wave in the two layers.

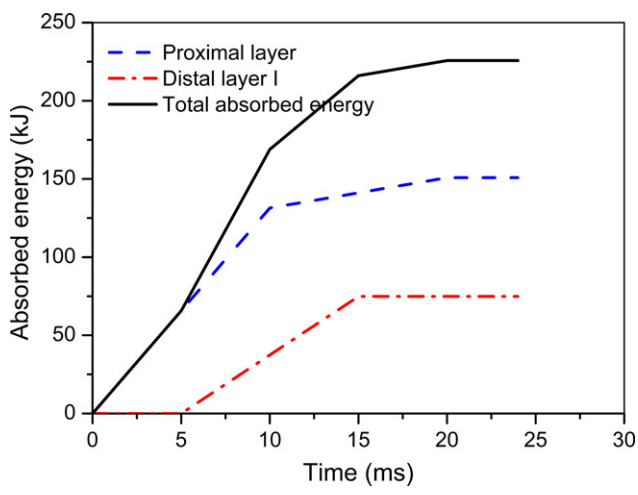

Figure 12. Time histories of absorbed energy in Scenario II.

4. Discussion

4.1. Analysis on the velocity platform phenomena

The histories of the interface velocities present a platform phenomenon that the velocity jumps at the start of every two stages and keep almost constant in each stage as shown in Figures 7 and 10. The reason for this phenomenon is discussed in this section.

The interfaces are joints of two different materials. Thus, their response should satisfy the properties of both two materials. Consider interface A_1 as an example. After the onset of impact, an elastic precursor wave reaches A_1 with an infinite speed and then the stress and velocity of interface A_1 rise simultaneously. On the one hand, the stress and velocity of interface A_1 need to satisfy Eq. (4) as required by the stress wave theory for the elastic rod. On the other hand, if we consider the uncompacted part of the proximal layer, the stress at the left side is σ_{01} and that on the right side is the stress of interface A_1. It is the difference of the stresses on the two sides makes

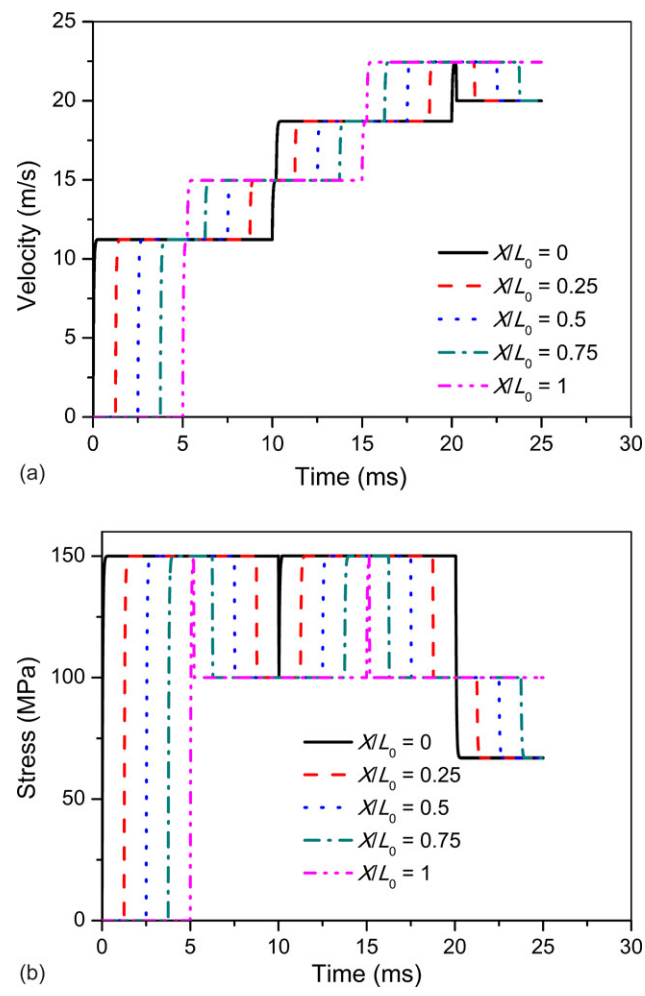

Figure 13. Time histories of velocity (a) and stress (b) for Scenario II at selected Lagrange locations in the elastic rod.

the uncompacted part accelerates, which leads to the increase of the velocity of interface A_1. As long as the stress of the interface A_1 is lower than σ_{01}, the acceleration process continues but, due to the increase of the stress at the interface, the acceleration reduces. The initial acceleration can be expressed as $\sigma_{01}/(\rho_1 L_1)$, while the characteristic velocity associated with σ_{01} is $\sigma_{01}C_0/E$ according to Eq. (4). Thus, the characteristic rise time of the stress and velocity of the interface A_1 can be expressed as $\rho_1 L_1 C_0/E$. By contrast, the characteristic time for the stress wave propagation in the elastic rod is Δt defined by Eq. (7). So, a platform phenomenon in the velocity and stress histories of the interface A_1 occurs when the characteristic rise time is much less than the characteristic time for the stress wave propagation, that is when

$$\frac{\rho_1 L_1}{\rho_0 L_0} \ll 1. \tag{42}$$

This is true for the present case and the value of $\rho_1 L_1/\rho_0 L_0$ is 8.9×10^{-3} in this study. Actually, the characteristic time of the stress and velocity rise is 0.045 ms while that of the wave propagation is 5.06 ms, more than one hundred times larger than the former. Similar results can be obtained for other interfaces.

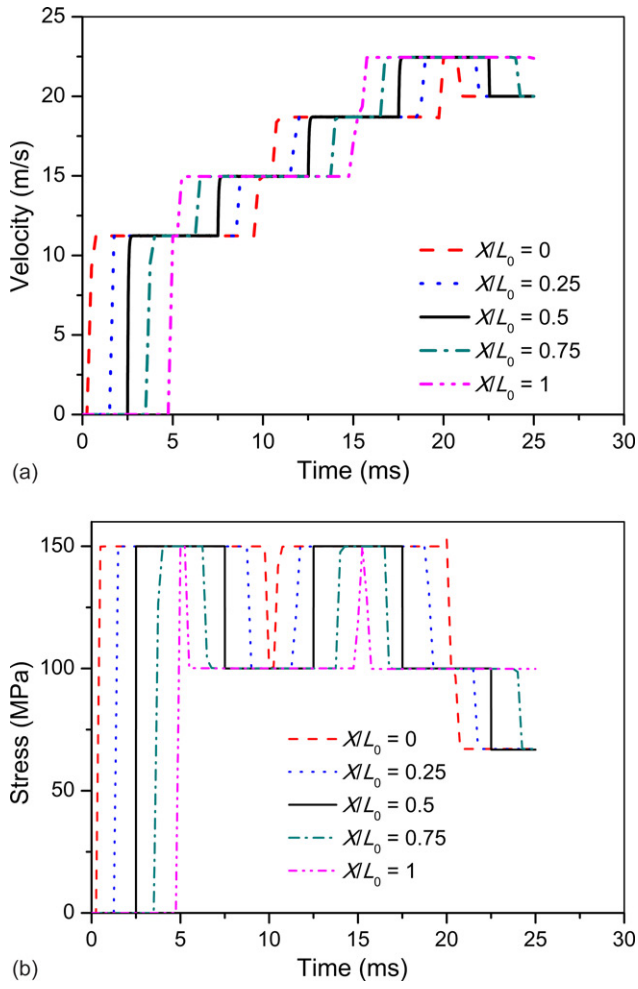

Figure 14. A comparison between the theoretical predictions and FE results of velocity (a) and stress (b) for selected Lagrangian locations in the elastic rod.

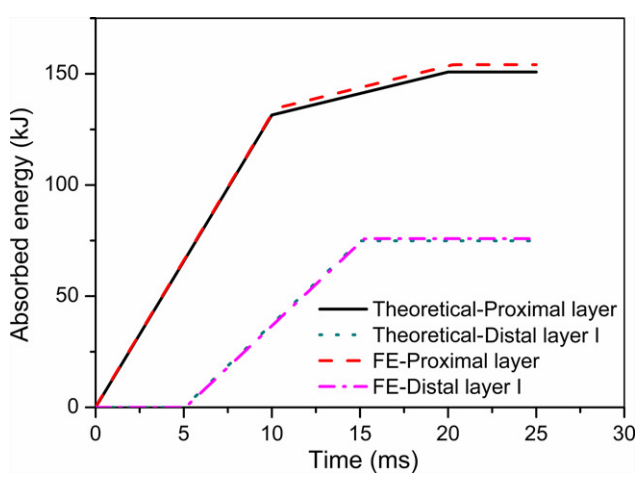

Figure 15. A comparison between the theoretical predictions and FE results of the absorbed energy.

4.2. Condition for the end of crushing

In general, when a layer is fully compacted or the velocities of its two interfaces reach the same, the layer stops crushing. In the latter case the layer may be partially compacted but for both cases the layer becomes rigid, and the stresses on the two interfaces become identical, which may decrease or increase due to the wave acting on the interface. The layer will maintain rigid body unless the interfacial stress reaches the crushing stress again. When all layers stop crushing, the energy absorption process finishes. This depends on the composition and parameters of the system as well as the impact velocity. Different situations may occur during the response. As analyzed in the last section, each interface should meet a certain stress condition during crushing, which is the key factor.

4.3. Simplified analysis procedure and expression

Based on the above analysis, in each stage, the velocity of an interface is determined by the stress of the interface, the Young's modulus and density of the connecting rod and the reflected wave from the other end of the elastic rod. The whole moving process of each interface consists of a transient acceleration process at the initial stage and a following nearly constant velocity process. If we ignore the acceleration process, the velocity of the interfaces in each stage depends only on the plateau stress of the two layers

and the Young's modulus and density of elastic rods by a set of equations.

Here, we take Scenario II as an example to discuss the simplified expressions. The velocity of interface A_1 changes only at the start of odd stages and those of interface A_2 and interface A_3 change only at the start of even stages, and then keep constant for two stages. Therefore, simplified expressions of the velocities of interface A_1, A_2 and A_3 during crushing can be obtained respectively as

$$v_{A1}^{(2j-1)} = \frac{C_0}{E}[(2j-1)\sigma_{01} - 2(j-1)\sigma_{02}], \tag{43}$$

$$v_{A2}^{(2j)} = \frac{C_0}{E}[2j\sigma_{01} - (2j-1)\sigma_{02}], \tag{44}$$

and

$$v_{A3}^{(2j)} = \frac{C_0}{E}(2j-1)\sigma_{02}, \tag{45}$$

where the superscripts denote the numbers of stages and j is a positive integer.

Then, simplified expressions of Lagrangian speeds of the compaction wave in the two layers are gained by Eqs. (5) and (24) together with Eqs. (43)–(45):

$$v_{\Phi1}^{(2j-1)} = \frac{V}{\varepsilon_d} - \frac{C_0}{E\varepsilon_d}[(2j-1)\sigma_{01} - 2(j-1)\sigma_{02}] \tag{46}$$

and

$$v_{\Phi2}^{(2j)} = \frac{2C_0}{E\varepsilon_d}[j\sigma_{01} - (2j-1)\sigma_{02}], \tag{47}$$

which can be used to judge whether crush stops in a certain stage and to estimate the crush length. Then, the maximum value of j for each layer, denoted as J_1 and J_2, can be determined.

During crushing, the stress behind the compaction wave front does not rise up significantly because the cases studied are low velocity impact. Therefore, a further simplification can be made by assuming that the stress behind the compaction wave front is approximately equal the plateau stress of the layer. For the R-PP-L shock model is employed to investigate the response of materials in the two layers, we consider that the part swept by compaction wave become compacted at once. Therefore, the absorbed energy can be expressed as a product of plateau stress, strain of compaction, crushed length and sectional area. The crushed lengths of the two layers can be obtained with Lagrangian speeds of the compaction in each stage. As analyzed above, the absorbed energy of the two layers can be expressed as

$$E_1 = 2\Delta t \sum_{j=1}^{J_1} \left\{ V - \frac{C_0}{E}[(2j-1)\sigma_{01} - 2(j-1)\sigma_{02}] \right\} \sigma_{01} s \tag{48}$$

and

$$E_2 = 2\Delta t \sum_{j=1}^{J_2} \frac{2C_0}{E}[j\sigma_{01} - (2j-1)\sigma_{02}]\sigma_{02} s. \tag{49}$$

A comparison of the absorbed energy predicted by the theoretical solutions and the simplified expressions is shown in Figure 16.

4.4. The necessity of considering elastic wave effect

To demonstrate the necessity of considering the elastic wave effect in the analysis of a distributed energy absorption system, a reference model is used which just replaces the elastic connecting rod to a rigid rod while all the other parameters are the same as those for Scenario I. When impact occurs, the compaction wave starts to propagate in the proximal layer. In the meanwhile, an elastic precursor wave initiates and travels through the proximal layer and the rigid rod with an infinite speed. The distal layer starts to be crushed at the same time. The undeformed part of the proximal layer, the rigid rod and the compacted part of the distal layer move with the same speed. The governing equations are formulated with respect to the velocity v_1 of the rigid rod and the thickness of the compaction lengths Φ_3 and Φ_4 in the proximal and distal layers respectively. We have

$$\frac{d\Phi_3}{dt} = \frac{V - v_1}{\varepsilon_d}, \tag{50}$$

$$\frac{dv_1}{dt} = \frac{\sigma_{01} - \rho_2 v_1^2/\varepsilon_d}{\rho_1(L_1 - \Phi_3) + \rho_0 L_0 + \rho_2 \Phi_4} \tag{51}$$

and

$$\frac{d\Phi_4}{dt} = \frac{v_1}{\varepsilon_d}, \tag{52}$$

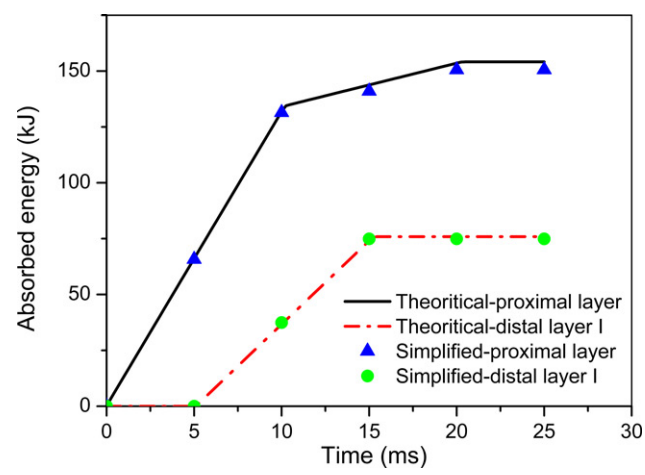

Figure 16. Comparison of the theoretical result with that of simplified expressions.

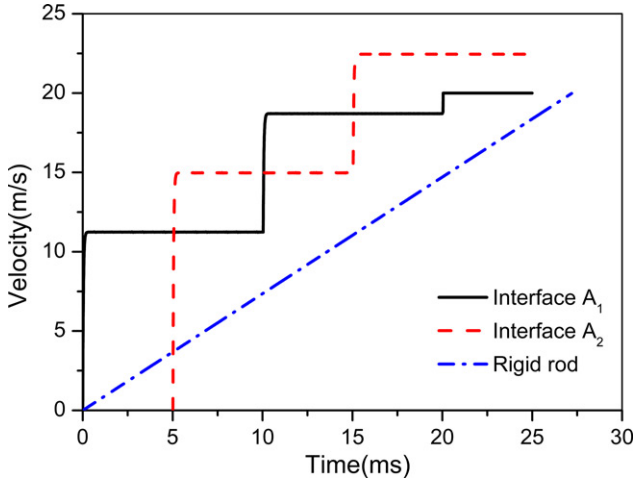

Figure 17. Time histories of velocities of interface *A*1, interface *A*2 and the rigid rod.

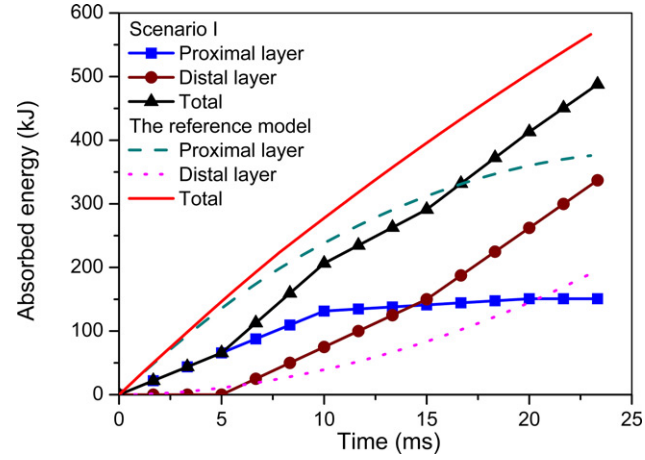

Figure 18. Variation of the absorbed energy of the two layers for Scenario I and the reference model.

with the initial conditions $\Phi_3(0) = 0, v_1(0) = 0$ and $\Phi_4(0) = 0$.

The governing equations for the reference model are numerically solved. Typical time histories of the velocities of interface A_1 and interface A_2 of Scenario I and that of the rigid rod in the reference model are shown in Figure 17. As can be seen from the results, the velocity of the rigid body in the reference model increases almost linearly.

Because the Lagrangian speeds of the compaction wave in the two energy absorption layers depends on the interface velocity, it is expected that the Lagrangian speeds of the compaction wave in the two layers and furthermore the absorbed energy predicted by the present theoretical model and the reference model exhibit different features. The absorbed energy of the two layers for reference model can be solved by Eqs. (40) and (41), where the stress just behind the collapsing wave front and the Lagrangian speeds of the compaction wave can be obtained similarly to the present theoretical model. The variation of the absorbed energy of the two layers for Scenario I and the reference model is shown in Figure 18.

For comparing the results of Scenario I and the reference model as shown in Figure 16, the energy absorption processes are totally different. First, the two layers in the reference model start to be crushed at the same time but in the theoretical model with a time interval. That reflects the pattern of 'step by step to trigger' in a distributed energy absorption system. Second, the absorbed energy of Scenario I increases linearly with time in each stage and that of the reference model takes the form of quadratic curve throughout the process, which correspond to their Lagrangian speeds of the compaction waves. Third, the absorbed energy of Scenario I is lower in the proximal layer and higher in the distal layer than that of the reference model, which can bring in difference of the distribution of energy absorption. Fourth, the total energy absorption of Scenario I is obviously lower than that of reference model. In general, both rising tendency and final energy absorption in the two layers of two models are different. If elastic wave effect is not considered, the energy absorption capability of a distributed energy absorbing system will be overestimated, and the contribution of each energy absorber will be erroneously estimated. As discussed above, the introduction of elastic wave effect is necessary for the analysis on distributed energy absorption system.

5. Conclusions

In this article, a simplified one-dimensional theoretical model considering elastic wave effect is introduced to analyze the distributed energy absorbing system of train. Three collision scenarios are discussed.

The compaction wave motion in the energy absorber layer is analyzed using shock wave theory. By dividing the process into several stages, the analysis is reduced to solve a set of ordinary deferential equations in each stage for the stress and velocities at the interfaces. The response and energy absorption of two collision scenarios are presented. A platform phenomenon of response in all stages is observed. It is shown that ignoring the elastic wave effect will lead to an overestimate of the energy absorption capability and wrong estimate of the contribution of individual energy absorber. The theoretical predictions are verified by FE method with ABAQUS/Explicit code. Finally, a simplified approximate analysis procedure is proposed.

The present method can be adopted for various collision scenarios by just changing the system

components and impact conditions. Therefore, the model and analysis method presented in this article are expected to be used for the analysis of coordination of energy absorber components and for the preliminary design and optimization of the distributed energy absorbing system.

Note

1. Normally there are two energy absorbers at the two ends of a carriage. For simplicity, we put the energy absorbers between the nearby carriages together into the back end.

Disclosure statement

No potential conflict of interest was reported by the authors.

Funding

The research reported herein is supported by the National Natural Science Foundation of China (Project No. 11372307), which is gratefully acknowledged.

References

[1] Edkins GD, Pollock CM. Pro-active safety management: application and evaluation within a rail context. Safety Sci. 1996;24:83–93.
[2] Shao F, Li K. A graph model for preventing railway accidents based on the maximal information coefficient. Int J Mod Phys B. 2016;31:1750010.
[3] Drazetic P, Tassin R, Ravalard Y, et al. Experimentation and modelling of climbing phenomena of guided transport vehicles. Proc Inst Mech Eng F J Rail Rapid Transit. 1995;209:11–17.
[4] Contri P, Gürpinar A, Schneider U. Optimal design of train structures for crashworthiness using a multiload approach. Int J Crashworthiness. 2002;7:331–344.
[5] Dias JP, Pereira MS. Optimization methods for crashworthiness design using multibody models. Comput Struct. 2004;82:1371–1380.
[6] Duan L, Sun G, Cui J, et al. Crashworthiness design of vehicle structure with tailor rolled blank. Struct Multidiscipl Optim. 2016;53:321–338.
[7] Gao GJ, Tian HQ. Train's crashworthiness design and collision analysis. Int J Crashworthiness 2007;12: 21–28.
[8] Jacobsen K, Parent D. Preparations for a train-to-train impact test of crash-energy management passenger rail equipment, in Rail Conference, 2005. Proceedings of the 2005 ASME/IEEE Joint; 2005. p. 107–116.
[9] Jacobsen K, Severson K, Perlman B. Effectiveness of alternative rail passenger equipment crashworthiness strategies, in Rail Conference, 2006. Proceedings of the 2006 IEEE/ASME Joint; 2006. p. 121–129.
[10] Tyrell D, Perlman AB. Evaluation of rail passenger equipment crashworthiness strategies. Transport Res Rec J Transport Res Board. 2003;1825:8–14.
[11] Kirkpatrick SW, Schroeder M, Simons JW. Evaluation of passenger rail vehicle crashworthiness. Int J Crashworthiness. 2001;6:95–106.
[12] Simons J, Kirkpatrick S. High-speed passenger train crashworthiness and occupant survivability. Int J Crashworthiness. 1999;4:121–132.
[13] Belingardi G, Cavatorta MP, Duella R. Material characterization of a composite–foam sandwich for the front structure of a high speed train. Comp Struct. 2003; 61:13–25.
[14] Hu D, Wang Y, Song B, et al. Energy absorption characteristics of a foam-filled tri-tube under axial quasi-static loading: experiment and numerical simulation. Int J Crashworthiness. 2017:1–16. DOI: 10.1080/13588265.2017.1331494
[15] Li SY, Zheng ZJ, Yu JL. Energy-absorbing structure design and crashworthiness analysis of high-speed trains (in Chinese). Explosion Shock Waves 2015;35:164–170.
[16] Ambrósio JAC, Pereira MFOS, Dias JP. Distributed and discrete nonlinear deformations on multibody dynamics. Nonlinear Dyn. 1996;10:359–379.
[17] Han H, Koo J. Simulation of train crashes in three dimensions. Vehicle Syst Dyn. 2003;40:435–450.
[18] Milho JF, Ambrósio JAC, Pereira MFOS. Validated multibody model for train crash analysis. Int J Crashworthiness. 2003;8:339–352.
[19] Pereira M, Ambrosio J, Dias J. Crashworthiness analysis and design using rigid-flexible multibody dynamics with application to train vehicles. Int J Numer Methods Eng. 1997;40:655–687.
[20] Karagiozova D, Alves M. Stress waves in layered cellular materials – dynamic compaction under axial impact. Int J Mech Sci. 2015;101/102:196–213.
[21] Liao SF, et al. A design guide of double-layer cellular claddings for blast alleviation. Int J Aerosp Lightweight Struct. 2012;3:109–133.
[22] Reid SR, Peng C. Dynamic uniaxial crushing of wood. Int J Impact Eng. 1997;19:531–570.